Comparing three approaches to the inducing source setting for the ground electromagnetic field modeling due to space weather events

Elena Marshalko[1,2,3], Mikhail Kruglyakov[1,4], Alexey Kuvshinov[1], Liisa Juusola[5], Norah Kaggwa Kwagala[6], Elena Sokolova[2], Viacheslav Pilipenko[2,3]

[1]Institute of Geophysics, ETH Zürich, Zürich, Switzerland
[2]Institute of Physics of the Earth, Moscow, Russia
[3]Geophysical Center, Moscow, Russia
[4]Geoelectromagnetic Research Center, Institute of Physics of the Earth, Moscow, Russia
[5]Finnish Meteorological Institute, Helsinki, Finland
[6]Space Plasma Physics Group, Department of Physics and Technology, University of Bergen, Bergen, Norway

Key Points:

- 3-D electromagnetic field modeling is performed for Fennoscandia exploiting three different inducing source models
- Magnetic field perturbations are reproduced much more accurately using the SECS source than using the source based on MHD simulation outputs
- The difference between geoelectric fields modeled using laterally nonuniform source and plane wave approach is substantial in Fennoscandia

Corresponding author: Elena Marshalko, elena.e.marshalko@gmail.com

Abstract

Ground-based technological systems, such as power grids, can be affected by geomagnetically induced currents (GIC) during geomagnetic storms and magnetospheric substorms. This motivates the necessity to numerically simulate and, ultimately, forecast GIC. The prerequisite for the GIC modeling in the region of interest is the simulation of the ground geoelectric field (GEF) in the same region. The modeling of the GEF in its turn requires spatio-temporal specification of the source which generates the GEF, as well as an adequate regional model of the Earth's electrical conductivity. In this paper we compare results of the GEF (and ground magnetic field) simulations using three different source models. Two models represent the source as a laterally varying sheet current flowing above the Earth. The first model is constructed using the results of a physics-based 3-D magnetohydrodynamic (MHD) simulation of near-Earth space, the second one uses ground-based magnetometers' data and the Spherical Elementary Current Systems (SECS) method. The third model is based on a "plane wave" approximation which assumes that the source is locally laterally uniform. Fennoscandia is chosen as a study region and the simulations are performed for the 7-8 September 2017 geomagnetic storm. We conclude that ground magnetic field perturbations are reproduced more accurately using the source constructed via the SECS method compared to the source obtained on the basis of MHD simulation outputs. We also show that the difference between the GEF modeled using laterally nonuniform source and plane wave approximation is substantial in Fennoscandia.

1 Introduction

Large coronal mass ejections from the Sun release massive amounts of plasma, which flow at high speed into the interplanetary space. The interaction of this solar wind with the Earth's magnetosphere can lead to significant spatio-temporal disturbances of the magnetic field at the surface of the Earth, which are known as geomagnetic storms. These space weather events induce a geoelectric field (GEF) in the Earth's subsurface, which in turn drives geomagnetically induced currents (GIC) in ground-based technological systems such as power grids and pipelines posing a significant risk to the reliability and durability of such infrastructure.

The core component in quantitative estimation of the hazard to technological systems from space weather is as realistic as practicable numerical modeling of GIC, and, ultimately, their forecasting. Ideally, to perform GIC modeling one needs the following ingredients: a) a realistic model of the source of geomagnetic disturbances; b) a comprehensive three-dimensional (3-D) electrical conductivity model of the Earth's subsurface in the region of interest; c) a 3-D numerical solver which allows for accurate and detailed modeling of the GEF in a given conductivity model excited by a given source; d) the geometry of transmission lines and system design parameters that allow for the conversion of the modeled GEF into GIC.

Many previous studies in connection with GIC operated with simplified models either of conducting Earth (one-dimensional (1-D) or thin sheet conductivity models) or the source (vertically propagating laterally uniform electromagnetic (EM) field; plane wave), or both (e.g., Viljanen et al. (2012, 2013, 2014); Püthe and Kuvshinov (2013); Püthe et al. (2014); Beggan et al. (2013); Beggan (2015); Kelly et al. (2017); Honkonen et al. (2018); Bailey et al. (2017, 2018); Divett et al. (2017, 2020)).

In spite of the fact that the importance of performing simulations using fully 3-D conductivity models is currently widely recognised (Kelbert, 2020), such simulations are still rather rare in the GIC community (e.g., Wang et al. (2016); Pokhrel et al. (2018); Nakamura et al. (2018); Liu et al. (2018); Marshall et al. (2019); Rosenqvist and Hall (2019); Marshalko et al. (2020)), mostly due to the lack of the credible 3-D conductiv-

ity models of the regions of interest as well as unavailability of adequate tools to model the problem in the full complexity.

As for the source, approximating it by plane waves still prevails in the GIC-related studies (e.g., Kelbert et al. (2017); Kelbert and Lucas (2020); Lucas et al. (2018); Campanya et al. (2019); Sokolova et al. (2019); Wang et al. (2020)). This approximation seems reasonable in low and middle latitudes, where the main source of anomalous geomagnetic disturbances is a large-scale magnetospheric ring current. However, the plane wave assumption may not work in higher latitudes, where the main source of the disturbances is the auroral ionospheric current, which is extremely variable both in time and space, especially during periods of enhanced geomagnetic activity (Belakhovsky et al., 2019). Marshalko et al. (2020) provided some evidence for that by comparing ground EM fields modeled in the eastern United States using the plane wave approximation and the excitation by a laterally variable source which was constructed using outputs from 3-D magnetohydrodynamic (MHD) simulation of near-Earth space. The authors found that the difference increases towards higher latitudes where the lateral variability of the source expectedly enlarges. However their modeling was mostly confined to mid-latitude region, thus it is still unclear how pronounced the difference between the plane wave and "laterally varying source" results could be in auroral regions. In this paper we investigate this problem using Fennoscandia as a study region. The choice of Fennoscandia is motivated by: a) high-latitude location of the region; b) the availability of the 3-D ground electrical conductivity model of the region (Korja et al., 2002) c) the existence of the regional magnetometer network (International Monitor for Auroral Geomagnetic Effect, IMAGE (Tanskanen, 2009)) allowing us to build data-based model of a laterally variable source, which is a natural alternative to physics-based (MHD) source model in the areas with a reasonably dense net of observations.

Specifically, we perform 3-D modeling of ground electric and magnetic fields in Fennoscandia using three different source models and taking 7–8 September 2017 geomagnetic storm as a space weather event. Two models approximate the source by laterally varying sheet current flowing above the Earth's surface. One of the models is built using the results of physics-based 3-D MHD simulation of the near-Earth space, another model uses the IMAGE magnetometer data and the Spherical Elementary Current Systems (SECS) method (Vanhamäki & Juusola, 2020; Juusola et al., 2020). The third modeling is based on a "plane wave" approximation which assumes that the source is locally laterally uniform. Note that previous GIC-related studies in Fennoscandia operated with both 1-D (e.g., Pulkkinen et al. (2005); Myllys et al. (2014); Viljanen and Pirjola (2017)) and 3-D (Rosenqvist & Hall, 2019; Dimmock et al., 2019, 2020) Earth's conductivity models, the magnetic field in most of these papers was allowed to be laterally variable, but the GEF was always calculated implicitly assuming the plane wave excitation.

We compare modeling results and discuss found differences and similarities. We also compare results of magnetic field modeling with observations. The paper is organized as follows. The methodology used is described in Section 2.1 followed by presentation of our results in Section 3. Finally, the discussion of our results and conclusions are given in Section 4.

2 Methodology

2.1 Governing equations and modeling scheme

We compute the electric, $\mathbf{E}(t, \mathbf{r})$, and magnetic, $\mathbf{B}(t, \mathbf{r})$, fields for a given Earth's conductivity distribution $\sigma(\mathbf{r})$ and a given inducing source $\mathbf{j}^{ext}(t, \mathbf{r})$, where t and $\mathbf{r} = (x, y, z)$ denote time and position vector, correspondingly. These fields obey Maxwell's equations, that are written in the time domain as

$$\frac{1}{\mu_0}\nabla \times \mathbf{B} = \sigma \mathbf{E} + \mathbf{j}^{ext}, \tag{1}$$

$$\nabla \times \mathbf{E} = -\frac{\partial \mathbf{B}}{\partial t}, \tag{2}$$

where μ_0 is the magnetic permeability of a free space. Note that this formulation of Maxwell's equations neglects displacement currents, which are insignificant in the range of periods considered in this study. We solve eqs (1)-(2) numerically using the following three-step procedure:

1. The inducing source $\mathbf{j}^{ext}(t, \mathbf{r})$ is transformed from the time to the frequency domain with a fast Fourier transform (FFT).

2. Maxwell's equations in the frequency domain

$$\frac{1}{\mu_0}\nabla \times \mathbf{B} = \sigma \mathbf{E} + \mathbf{j}^{ext}, \tag{3}$$

$$\nabla \times \mathbf{E} = i\omega \mathbf{B}, \tag{4}$$

   are numerically solved for the corresponding angular frequencies $\omega = 2\pi f$, using the scalable 3-D EM forward modeling code PGIEM2G (Kruglyakov & Kuvshinov, 2018), based on a method of volume integral equations (IE) with a contracting kernel (Pankratov & Kuvshinov, 2016).

   We would like to note here that in our previous papers (Ivannikova et al., 2018; Marshalko et al., 2020) we used modeling code *extrEMe* (Kruglyakov et al., 2016) which is also based on IE method. The distinction between two codes lies in different piece-wise bases used. PGIEM2G exploits a piece-wise polynomial basis whereas *extrEMe* uses a piece-wise constant basis. We found that in order to properly account for the effects (in electric field) from extremely large conductivity contrasts in the Fennoscandian region, *extrEMe* requires significantly larger computational loads compared to the PGIEM2G. This is the reason why we used the PGIEM2G code rather than *extrEMe* to obtain modeling results presented in this paper. Specifically, PGIEM2G was run with the use of first-order polynomials in lateral directions and third-order polynomials in the vertical direction.

   Frequencies f range between $\frac{1}{L}$ and $\frac{1}{2\Delta t}$ where L is the length of the (input) times series of the inducing current $\mathbf{j}^{ext}(t, \mathbf{r})$, and Δt is the sampling rate of this time series. In this study Δt is 1 min, and L is 8 h.

3. $\mathbf{E}(t, \mathbf{r})$ and $\mathbf{B}(t, \mathbf{r})$ are obtained with an inverse FFT of the frequency-domain fields.

2.2 3-D conductivity model

3-D conductivity model of the region was constructed using the SMAP (Korja et al., 2002) – a set of maps of crustal conductances (vertically integrated electrical conductivities) of the Fennoscandian Shield, surrounding seas, and continental areas. The SMAP consists of six layers of laterally variable conductance. Each layer has the thickness of 10 km. The first layer comprises contributions from the sea water, sediments, and upper crust. The other five layers describe conductivity distribution in the middle and lower crust. SMAP covers an area 0°E – 50°E and 50°N – 85°N and has $5' \times 5'$ resolution. We converted the original SMAP database into Cartesian 3-D conductivity model of Fennoscandia with three layers of laterally variable conductivity of 10, 20 and 30 km thicknesses (Figures 1.a-c). This vertical discretization is chosen to be compatible with that previously used by Rosenqvist and Hall (2019) and Dimmock et al. (2019, 2020) for

GIC studies in the region. To obtain the conductivities in Cartesian coordinates we applied the transverse Mercator map projection (latitude and longitude of the true origin are 50°N and 25°E, correspondingly) to original data and interpolated the results onto a regular lateral grid. The lateral discretization and size of the resulting conductivity model were taken as 5×5 km^2 and 2550×2550 km^2, respectively. Deeper than 60 km we used a 1-D conductivity profile obtained by Grayver et al. (2017) (cf. Figure 1.d).

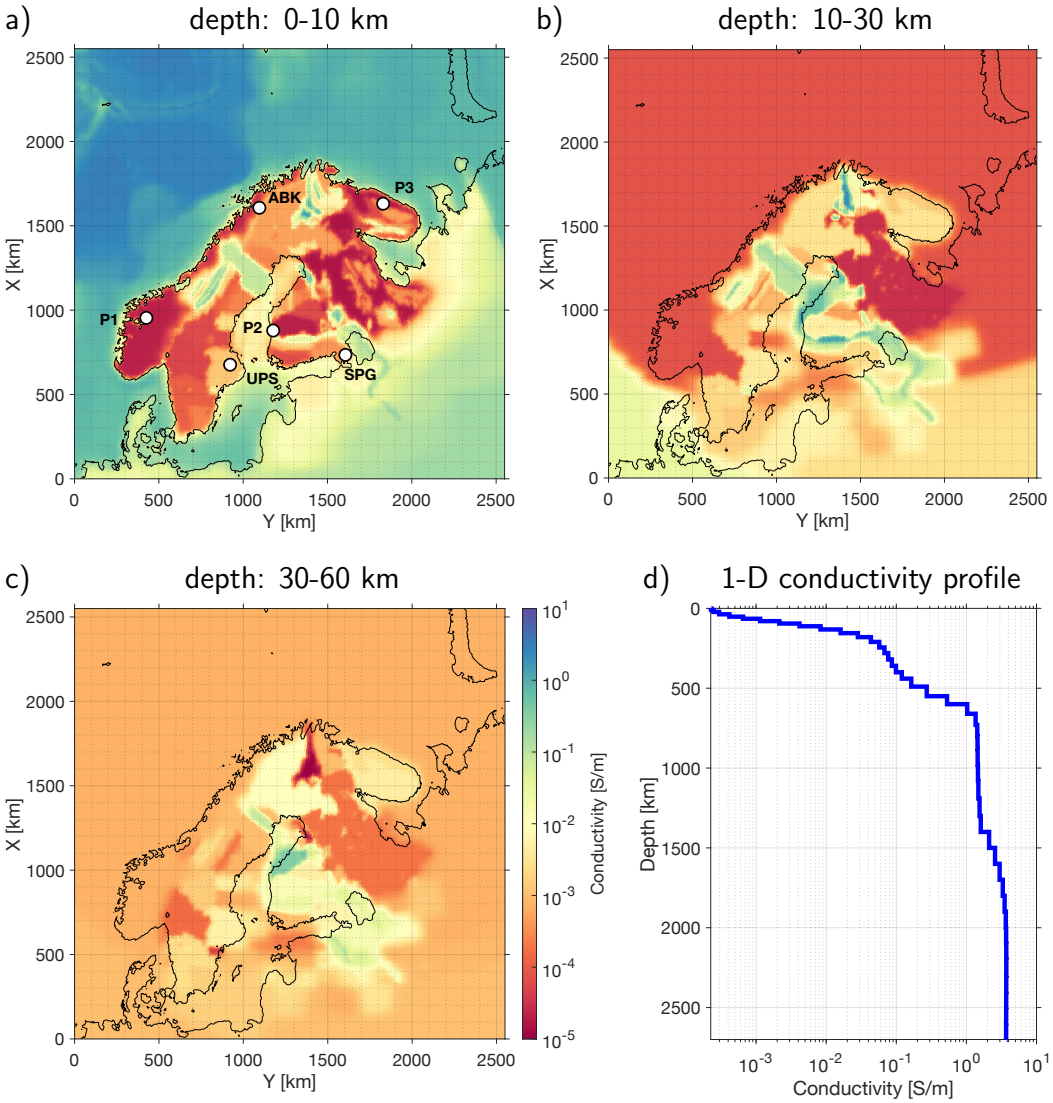

Figure 1. Conductivity distribution [S/m] in the model: a)–c) Plane view on 3 layers of the 3-D part of the model; d) global 1-D conductivity profile derived by Grayver et al. (2017) and used in this study. Locations of geomagnetic observatories Abisko (ABK), Uppsala (UPS), Saint Petersburg (SPG), and P1, P2 and P3 points are marked with circles in plot (a).

2.3 EM induction source settings

In this section we discuss the construction of two models for laterally variable source and also explain how EM field is calculated in the framework of plane wave (laterally uniform source) concept. The sources are set up for the geomagnetic storm on 7-8 Septem-

ber 2017, more specifically, for 8 hours time period from 20:00 UT, 7 September 2017 to 03:59 UT, 8 September 2017, thus, before and during the main phase of the storm. The disturbance storm time (Dst) index during this geomagnetic storm reached -124 nT according to the World Data Center of Kyoto (`http://wdc.kugi.kyoto-u.ac.jp/dstdir/`). More details on the September 2017 storm can be found in Linty et al. (2018) and Dimmock et al. (2019).

2.3.1 Construction of the source on the basis of an MHD simulation

The first source model is based on the results of physics-based 3-D MHD simulation of near-Earth space. In this study we employ the Space Weather Modeling Framework (SWMF, Toth et al. (2005, 2012)). The input to this MHD model are solar wind (density, temperature, velocity) and interplanetary magnetic field parameters measured at satellites located at L1 Lagrange point, such as Advanced Composition Explorer (ACE) and Deep Space Climate Observatory (DSCOVR). The other input is the solar radio flux at F10.7 cm (2800 MHz). The outputs are time-varying 3-D currents in the magnetosphere, horizontal currents in the ionosphere and field-aligned currents flowing between the magnetosphere and the ionosphere. These output data are then used to calculate (via the Biot-Savart law) external magnetic field perturbations $\mathbf{B}^{ext}(t, \mathbf{r})$ at the ground using the CalcDeltaB tool (Rastätter et al., 2014). Figure 2 demonstrates snapshots of the external magnetic field components at 23:16 and 23:52 UT on 7 September 2017 (during the main phase of the geomagnetic storm). Time series of the external magnetic field are computed globally at $5^\circ \times 5^\circ$ spatial grid with 1-min sampling rate and further converted into the equivalent current (stream) function $\Psi(t, \mathbf{r})$. The equivalent current density ($\mathbf{j}^{ext}(t, \mathbf{r})$ in eq. (1) is then calculated at the surface of the Earth based on the current function data as

$$\mathbf{j}^{ext} = -\delta(z - 0+)(\mathbf{e}_r \times \nabla_\perp \Psi), \tag{5}$$

where $\delta(z - 0+)$ is Dirac's delta function, $\mathbf{e}_r$ is the radial (outward) unit vector, and $\nabla_\perp$ is the surface gradient. The whole scheme of the equivalent current density calculation from the outputs of MHD simulations is discussed in Ivannikova et al. (2018).

The SWMF run, results of which are used in the current study, was performed at NASA's Community Coordinated Modeling Center (CCMC) at the Goddard Space Flight Center. The version of the SWMF is v20140611. The Rice Convection Model was used to simulate the inner magnetosphere dynamics (Toffoletto et al., 2003). The modeling domain consists of about 1 million grid cells. The size of the smallest cells is 0.25 R_E (where R_E is the Earth radius) close to the inner boundary of the modeling domain. The size of the largest cells is 8 R_E (close to the outer boundary in the distant tail). The outer boundaries are set at 32 R_E in the $+x$ upstream direction, 224 R_E in the $-x$ downstream direction, and 128 R_E in the $\pm y$ and z directions (GSM coordinates). The inner boundary is located at a distance of 2.5 R_E from the Earth's center. 1-min OMNI solar wind data have been used as an input in this run. The F10.7 cm flux was set to 130.4. Details and results of the run are available at the CCMC website (`https://ccmc.gsfc.nasa.gov`, run number `Naomi_Maruyama_011818_1`).

We would like to note that we also performed SWMF simulations with the same input parameters as were used in the CCMC `Naomi_Maruyama_011818_1` run, but with different spatial resolutions at the inner boundary of the modeling domain, namely, 0.125 and 0.0625 R_E. External magnetic fields (not shown in the paper) from higher-resolution MHD simulations appeared not to differ significantly from those obtained on the basis of `Naomi_Maruyama_011818_1` run in the region of our interest. Taking into account that small differences in external magnetic field should not notably affect modeling results, we construct the "MHD-based" source using `Naomi_Maruyama_011818_1` simulation outputs.

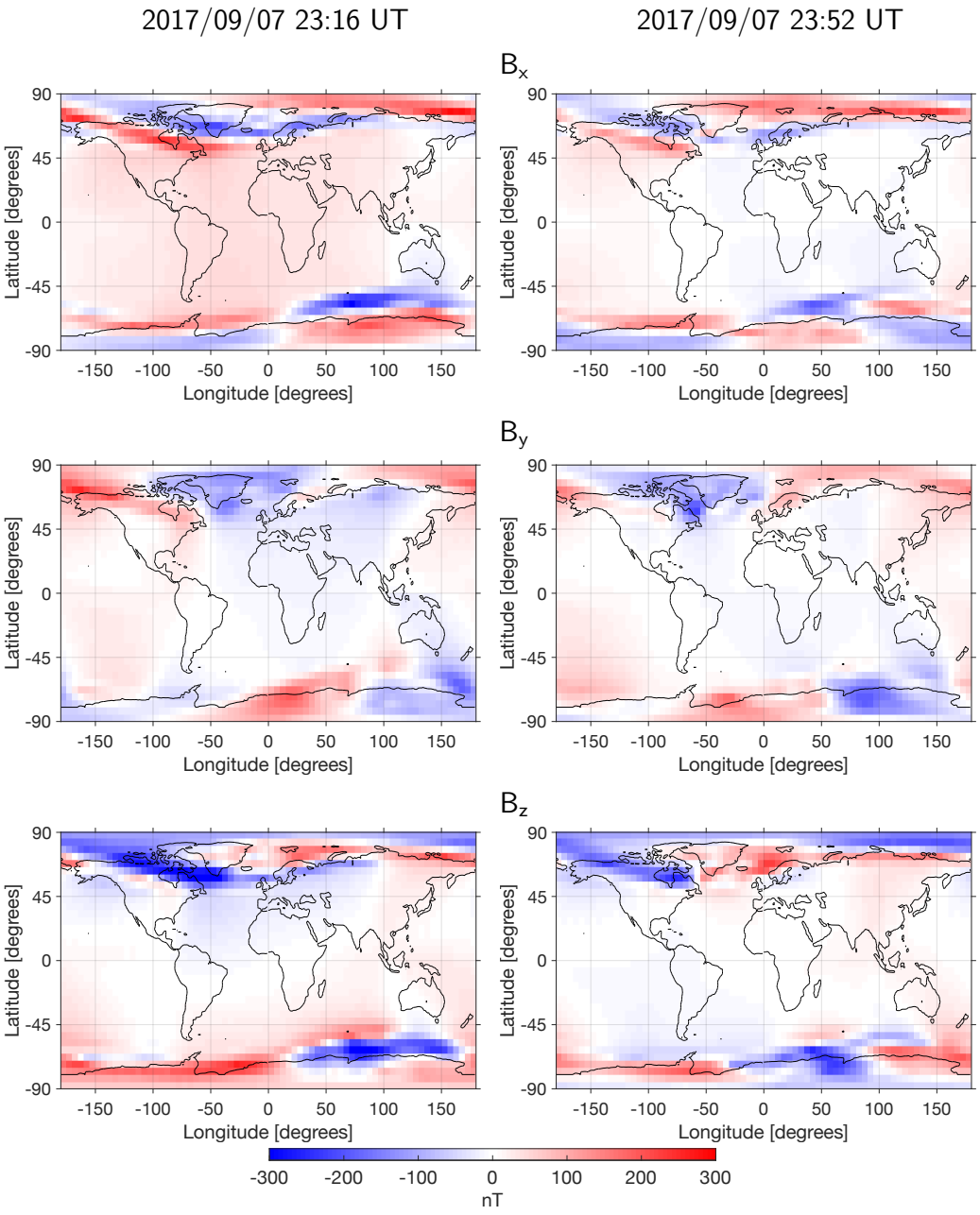

Figure 2. Global snapshots of the external magnetic field components at the surface of the Earth computed based on the SWMF outputs at 23:16 and 23:52 UT on 7 September 2017. B_x, B_y and B_z are northward, eastward and downward directed components, respectively.

2.3.2 Construction of the source using the SECS method

The second model of the source was constructed using the SECS method (Vanhamäki & Juusola, 2020). In this method the elementary current systems form a set of basis functions for representing two-dimensional vector fields on a spherical surface. An important application of the SECS method, which is relevant for this study, is the estimation of the ionospheric current system from ground-based measurements of magnetic field distur-

bances. Note that elementary current systems, as applied to ionospheric current systems, were first introduced by Amm (1997).

With the help of the SECS technique it is possible to separate the measured magnetic field into external and internal parts, which are represented by two equivalent sheet currents placed in the ionosphere and underground (Juusola et al., 2020).

To construct the external sheet current we have used IMAGE 10 s vector magnetic field data from all available stations, except for Røst and Harestua, for which the baselines are not yet determined. Baselines are subtracted from variometers' measurements according to the method of van de Kamp (2013). Ionospheric current density is computed using the 2-D SECS method (Vanhamäki & Juusola, 2020) with the following parameters:

- Altitude of the ionospheric equivalent current sheet: 90 km;
- Depth of the induced telluric equivalent current sheet: 0.001 km;
- Latitude resolution of the SECS grid: 0.5°;
- Longitude resolution of the SECS grid: 1°;
- Latitude range of the grid: from 59°N to 79°N;
- Longitude range of the grid: from 4°E to 42°E;

Note that extrapolation of the equivalent current density up to 42°E is performed in order to cover the whole region of Fennoscandia, even though the estimates of equivalent current far from the stations are less reliable. This applies not only to estimates at areas outside of the region covered by the stations but also to estimates inside of the region covered by the stations at locations where the distances between the nearby station are large.

Figure 3 demonstrates snapshots of equivalent current components at 23:16 and 23:52 UT on 7 September 2017.

We further perform the equivalent current extrapolation in order to ensure its smooth decay outside the region covered by the data. This is done to avoid the occurrence of the artifacts from the edges of the current sheet. We also reduce the temporal resolution of the estimated equivalent current from 10 s to 1 min in order to perform comparison of modeling results obtained via the MHD- and SECS-based sources. We then project the current density onto a region of interest and perform vector rotation, which is required for the results' transition from spherical to Cartesian coordinate system. After that we interpolate current density onto a regular Cartesian grid.

2.3.3 Plane wave modeling

The scheme of the GEF calculation via the plane wave approach differs from the one described in Section 2.1. The plane wave modeling results are obtained as follows:

1. 3-D EM forward modeling is carried out via PGIEM2G code (Kruglyakov & Kuvshinov, 2018) with two (laterally uniform) plane wave sources for the SMAP conductivity model at FFT frequencies corresponding to periods from 2 min to 8 h. 3-D MT impedances $Z(\mathbf{r},\omega)$ (Berdichevsky & Dmitriev, 2008) that relate the surface horizontal electric field with the surface magnetic field at each grid point $\mathbf{r}$

$$\mathbf{E}_h(\mathbf{r},\omega) = \frac{1}{\mu_0} Z(\mathbf{r},\omega)\mathbf{B}_h(\mathbf{r},\omega), \quad Z(\mathbf{r},\omega) = \begin{pmatrix} Z_{xx} & Z_{xy} \\ Z_{yx} & Z_{yy} \end{pmatrix}, \tag{6}$$

   are then calculated for each FFT frequency ω.
2. We then consider magnetic field modeled using the SECS-based source as the "true" magnetic field, thus mimicking the actual magnetic field in the region.

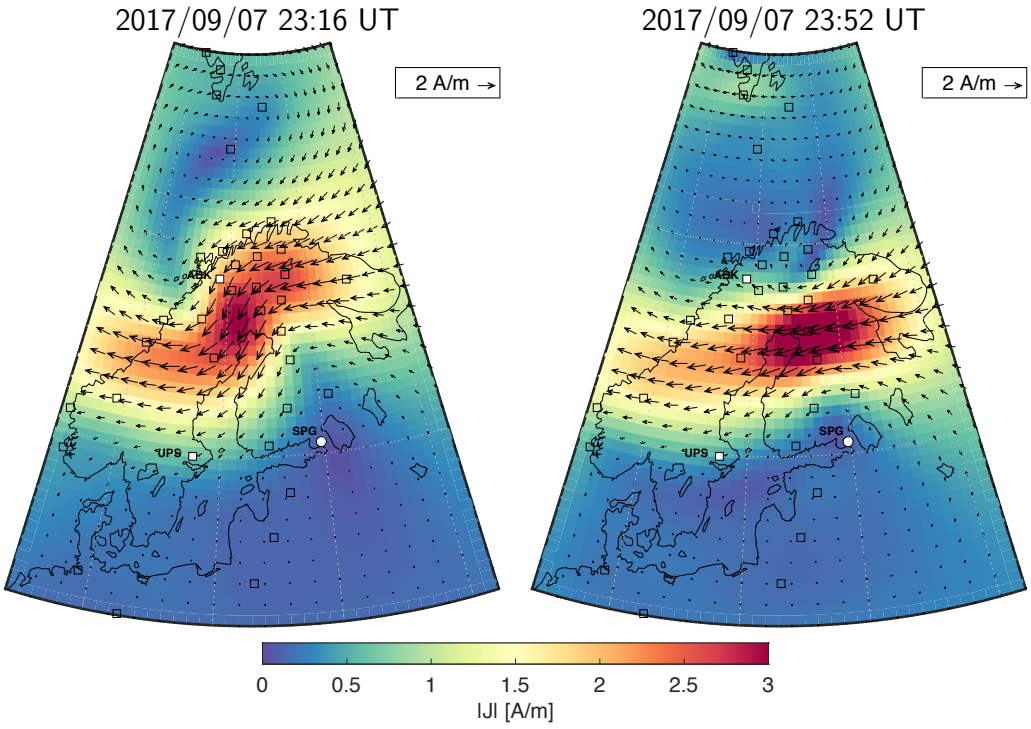

Figure 3. Snapshots of the magnitude and direction of the equivalent current computed using the SECS method at an altitude of 90 km above the surface of the Earth at 23:16 and 23:52 UT on 7 September 2017. Locations of IMAGE magnetometers (including Abisko (ABK) and Uppsala (UPS)), the data from which were used for the equivalent current construction, are marked with squares. Location of Saint Petersburg (SPG) geomagnetic observatory is marked with a circle. Note that SPG is not a part of the IMAGE magnetometers network and its magnetic field data were not used for the equivalent current construction.

3. Further, the horizontal GEF is calculated for each frequency and each grid point as

$$\mathbf{E}_h^{pw}(\mathbf{r}_s,\omega) = \frac{1}{\mu_0} Z(\mathbf{r},\omega)\mathbf{B}_h^{SECS}(\mathbf{r},\omega). \quad (7)$$

4. Finally, an inverse FFT is performed for the frequency-domain GEF to obtain the "plane wave" GEF in the time domain.

3 Results

3.1 Comparing results at a number of locations in the region

We first compare modeled and recorded magnetic field variations at the locations of the geomagnetic observatories Abisko (ABK), Uppsala (UPS), and Saint Petersburg (SPG) during the considered event. Observatories' locations are shown in Figure 1. The sampling rate of time series is 1 min. The linear trend was removed from observatory data before comparing them to modeling results.

Three upper plots in Figures 4-6 demonstrate time series of (total, i.e. external + induced) magnetic field modeled using MHD- and SECS-based sources (hereinafter to be referred as MHD-based and SECS-based magnetic fields), as well as time series of the observed magnetic fields. We do not show in these plots "plane wave" magnetic fields

Table 1. Normalized root-mean-square errors and correlation coefficients between SECS-based and observed magnetic field at Abisko (ABK), Uppsala (UPS) and Saint Petersburg (SPG) geomagnetic observatories. The results are shown for a time window from 20:00 UT, 7 September 2017 to 03:59 UT, 8 September 2017.

	ABK	UPS	SPG
nRMSE($B_{x,\mathrm{SECS}}$,$B_{x,\mathrm{obs}}$)	0.14	0.52	0.34
nRMSE($B_{y,\mathrm{SECS}}$,$B_{y,\mathrm{obs}}$)	0.32	0.5	1.17
nRMSE($B_{z,\mathrm{SECS}}$,$B_{z,\mathrm{obs}}$)	0.28	0.27	0.31
corr($B_{x,\mathrm{SECS}}$,$B_{x,\mathrm{obs}}$)	0.99	0.92	0.95
corr($B_{y,\mathrm{SECS}}$,$B_{y,\mathrm{obs}}$)	0.95	0.93	0.39
corr($B_{z,\mathrm{SECS}}$,$B_{z,\mathrm{obs}}$)	0.97	0.98	0.95

Table 2. The same legend as in Table 1 but for MHD-based magnetic field.

	ABK	UPS	SPG
nRMSE($B_{x,\mathrm{MHD}}$,$B_{x,\mathrm{obs}}$)	0.78	0.77	0.73
nRMSE($B_{y,\mathrm{MHD}}$,$B_{y,\mathrm{obs}}$)	1	1.25	1.06
nRMSE($B_{z,\mathrm{MHD}}$,$B_{z,\mathrm{obs}}$)	0.81	0.81	0.76
corr($B_{x,\mathrm{MHD}}$,$B_{x,\mathrm{obs}}$)	0.67	0.72	0.7
corr($B_{y,\mathrm{MHD}}$,$B_{y,\mathrm{obs}}$)	0.15	0.28	0.18
corr($B_{z,\mathrm{MHD}}$,$B_{z,\mathrm{obs}}$)	0.62	0.8	0.78

because by construction they coincide with SECS-based magnetic field (see the second item in Section 2.3.3). It is seen that the agreement between SECS-based and observed magnetic field for ABK and UPS observatories is very good in all components. This is not very surprising because magnetic field data from these observatories were used to construct the SECS source. As the construction is based on the least-square approach, it inevitably attempts to make predictions close to observations. In this context probably the most interesting comparison is for SPG observatory because this observatory is not a part of the IMAGE array, and its data were not used for the SECS source construction. Remarkably, the agreement between SECS-based and observed magnetic fields for SPG is also good, except B_y component. The disagreement in B_y may be due to a localized geomagnetic disturbance which is not accounted for in SECS source model. Table 1 supports quantitatively the above observations by presenting correlation coefficients between corresponding time series and the normalized root-mean-square errors which is defined as

$$\mathrm{nRMSE}(a,b) = \sqrt{\frac{\sum_{i=1}^{n}(a_i-b_i)^2}{n}} \Bigg/ \sqrt{\frac{\sum_{i=1}^{n} b_i^2}{n}}, \tag{8}$$

where a and b are modeled and observed time series, respectively, a_i and b_i are elements of these time series, and n is the number of these elements.

It is also seen from the Figures and Table 2 that the agreement between MHD-based and observed magnetic field is significantly worse for all considered observatories and all components. The agreement is especially bad in B_y component. On the whole the magnitude of MHD-based magnetic field perturbations is underestimated (compared to the

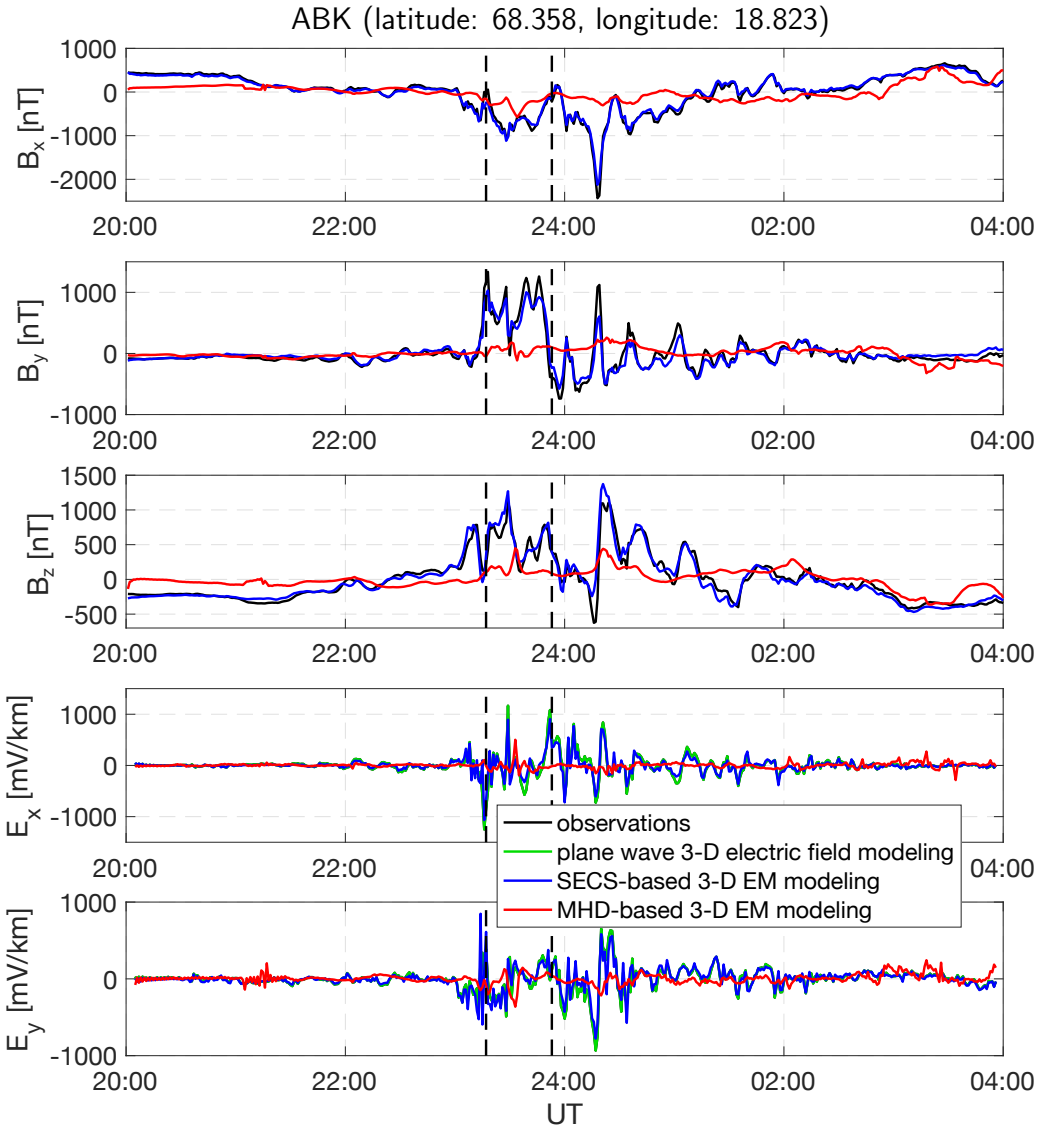

Figure 4. Three upper plots: modeled and observed time series of magnetic field at Abisko (ABK) geomagnetic observatory. Two lower plots: modeled time series of horizontal electric field. The results are shown for a time window from 20:00 UT, 7 September 2017 to 03:59 UT, 8 September 2017. Vertical dashed lines mark time instants (23:16 and 23:52 UT 7 September 2017) for which the results in Figures 2, 3 and 8-9 are shown.

SECS-based and observed magnetic field perturbations). Moreover, MHD-based magnetic field captures less of the short-period variability. These results are consistent with results of Kwagala et al. (2020), who carried out SWMF simulations for a number of space weather events and compared SWMF-based (external) magnetic fields with observed ones at a number of locations in northern Europe. According to their modeling results, the SWMF predicts the north-south component of external magnetic field perturbations better than the east-west component in auroral and subauroral regions, which is also the case in our modeling of the total magnetic field.

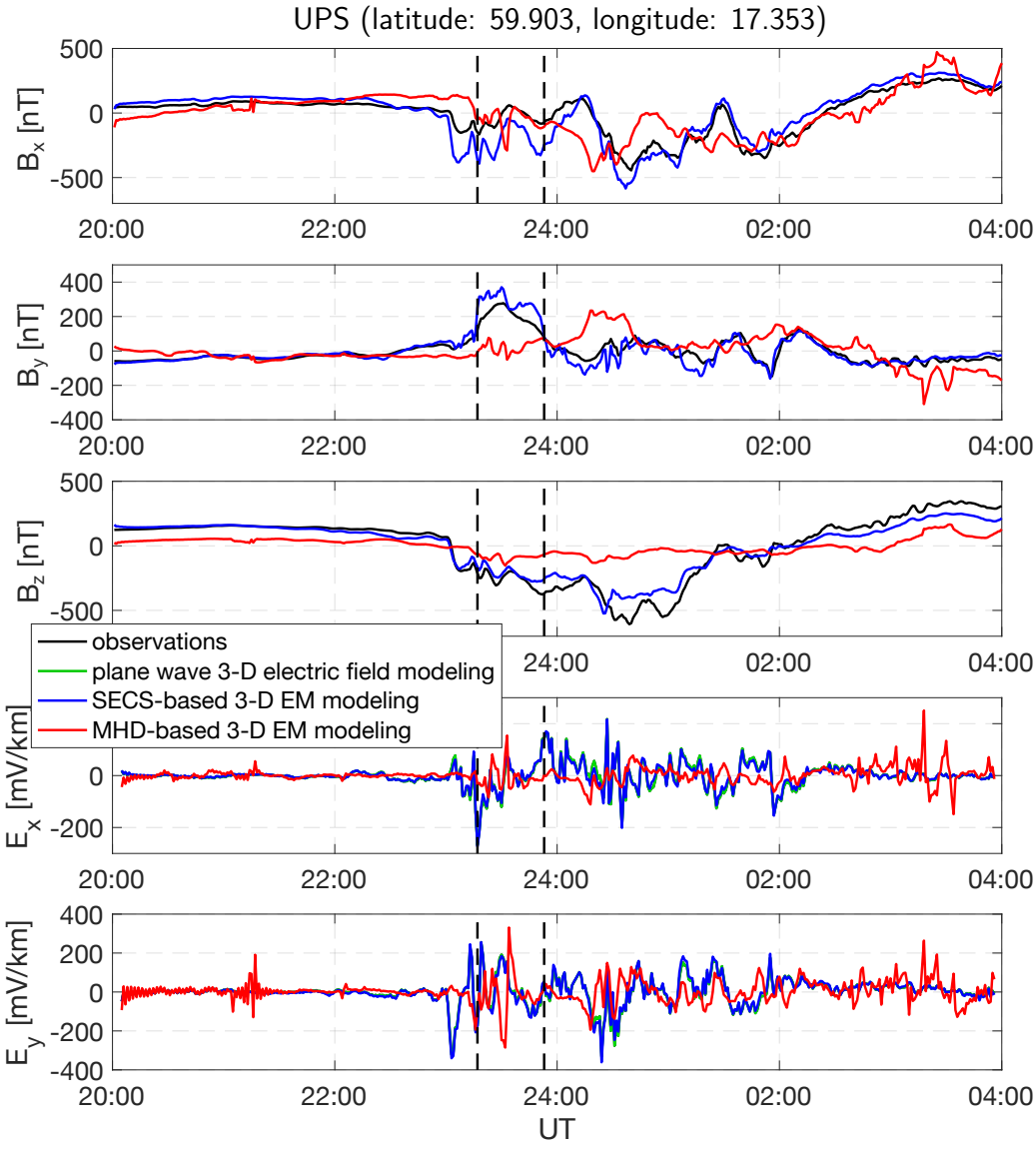

Figure 5. The same legend as in Figure 4 but for Uppsala (UPS) geomagnetic observatory.

Finally, two lower plots in Figures 4 - 6 show plane-wave-, SECS- and MHD-based horizontal GEF. Note that long-term continuous observations of GEF are absent in the region, thus only modeling results are shown in the plots.

Similarly to MHD-based magnetic field, the MHD-based GEF is underestimated compared to the SECS-based GEF. The correlation between these modeling results is very low and nRMSE are high (see Table 3).

On the contrary, SECS- and plane wave-based electric fields are rather close to each other, especially at locations of UPS and SPG observatories; Table 4 illustrates this quantitatively. Correlation between modeling results at ABK observatory is lower and nRMSE is higher most likely due to the fact that this observatory is situated in the region with high lateral conductivity contrasts (resistive landmass and conductive sea). To put more weight on this inference last three columns of Table 4 and Figure 7 demonstrate SECS- and plane-wave-based results for three "sites" also located in the regions with high lat-

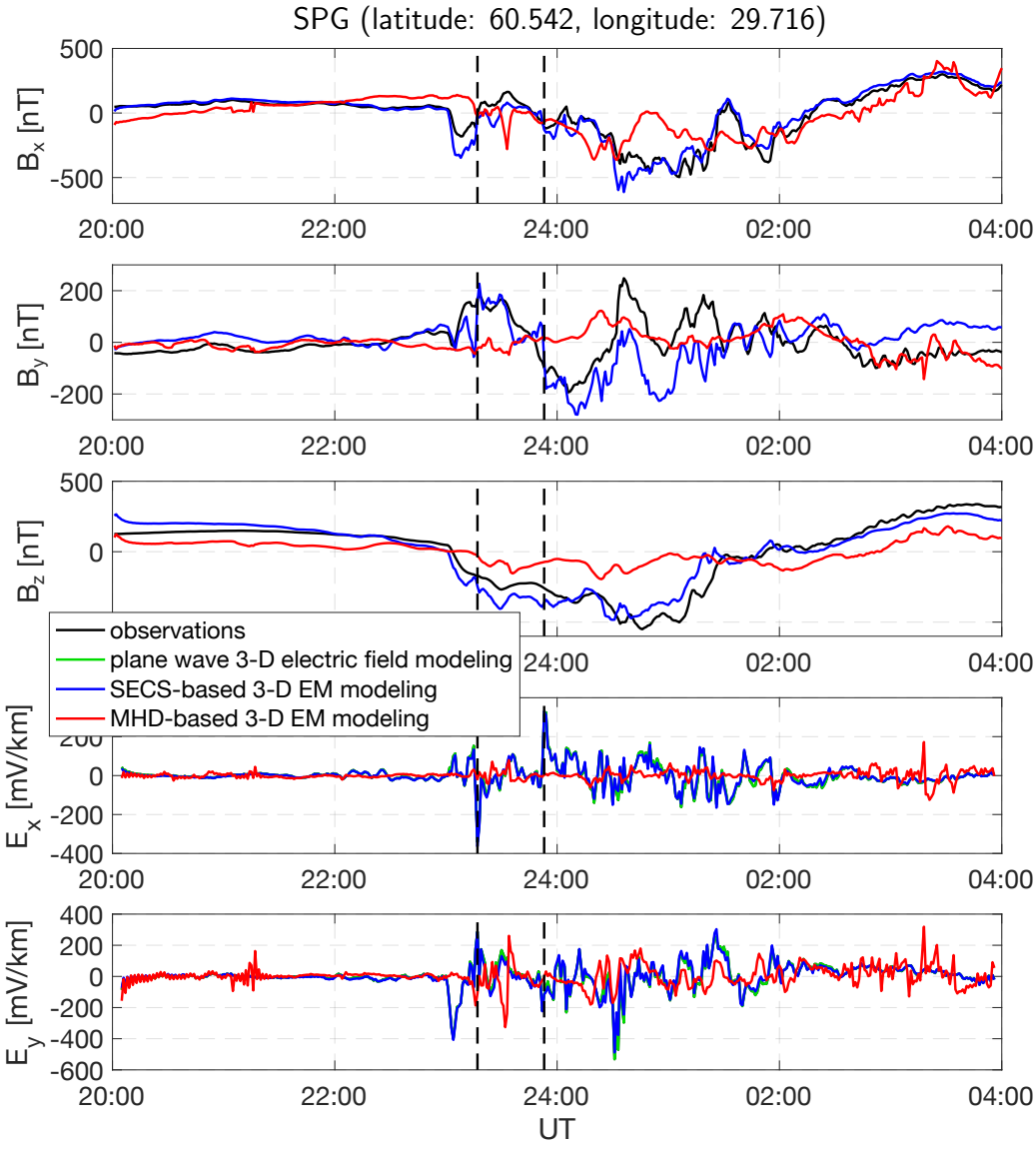

Figure 6. The same legend as in Figure 4 but for Saint Petersburg (SPG) geomagnetic observatory.

eral conductivity contrasts (their locations are shown in Figure 1). Now we observe that the difference between the results is even more pronounced which is, in particular, reflected in lower correlation coefficients and higher nRMSE.

3.2 Comparing results in the entire region

Contrary to previous section where we compared modeled and observed time series of EM field at a number of locations, in this section we compare MHD-, SECS- and plane-wave-based electric fields in the entire region for two time instants discussed earlier in the paper.

Top and middle plots in Figure 8 show magnitudes of respective SECS- and MHD-based GEF. Bottom plots show the absolute differences between corresponding GEF mag-

Table 3. The same legend as in Table 1 but for horizontal electric field.

	ABK	UPS	SPG
nRMSE($E_{x,\mathrm{MHD}}$,$E_{x,\mathrm{SECS}}$)	1.05	1.16	1.06
nRMSE($E_{y,\mathrm{MHD}}$,$E_{y,\mathrm{SECS}}$)	1.05	1.29	1.24
corr($E_{x,\mathrm{MHD}}$,$E_{x,\mathrm{SECS}}$)	0.001	0.12	0.06
corr($E_{y,\mathrm{MHD}}$,$E_{y,\mathrm{SECS}}$)	0.09	0.05	0.06

Table 4. The same legend as in Table 1 but for horizontal electric field, SECS- and plane-wave-based results and for three extra locations.

	ABK	UPS	SPG	P1	P2	P3
nRMSE($E_{x,\mathrm{SECS}}$,$E_{x,\mathrm{pw}}$)	0.42	0.16	0.17	0.85	0.81	0.83
nRMSE($E_{y,\mathrm{SECS}}$,$E_{y,\mathrm{pw}}$)	0.54	0.12	0.2	0.79	0.75	0.78
corr($E_{x,\mathrm{SECS}}$,$E_{x,\mathrm{pw}}$)	0.94	0.99	0.99	0.53	0.58	0.57
corr($E_{y,\mathrm{SECS}}$,$E_{y,\mathrm{pw}}$)	0.86	0.99	0.98	0.62	0.66	0.63

nitudes. It is seen that SECS-based GEF significantly exceeds MHD-based GEF throughout the Fennoscandian region and for both time instants. The largest differences occur in areas of strong lateral contrasts of conductivity (e.g., at the coast lines) and at higher latitudes.

In a similar manner, Figure 9 presents the comparison of SECS- and plane-wave-based GEF. In contrast to MHD-based results, at a first glance magnitude of plane-wave-based GEF is in overall comparable with SECS-based GEF (cf. top and middle plots in the figure). However, bottom plots show that the difference is substantial but more localized (compared to the difference between SECS- and MHD-based results), occurring, again, in areas of strong lateral contrasts of conductivity and increasing towards higher latitudes.

4 Conclusions and discussion

In this work we performed 3-D modeling of the EM field in the Fennoscandian region during the 7-8 September geomagnetic storm in 2017. The goal of this model study was to explore in what extent the resulting EM field depend on the setup of the external source which induces this field. We have used three different approaches to the EM induction source setting. The first technique is based on the retrieval of the (laterally variable) equivalent current from the dedicated MHD simulation. In the second method the laterally variable equivalent current is constructed on the basis of IMAGE magnetometers' data using the SECS approach. The third technique exploits plane wave concept, which implies that the source is laterally uniform locally.

Two main findings of the paper are as follows. Magnetic field perturbations in Fennoscandia are reproduced much more accurately using the SECS rather than MHD source. The difference between geoelectric fields modeled using SECS source and plane wave excitation is substantial in Fennoscandia, especially in the areas of strong lateral contrasts of conductivity (e.g. at the coasts), and at higher latitudes where lateral variability of the source becomes more pronounced.

From our study the reader may have a biased impression that the SECS-based current system is an ideal source candidate for rigorous modeling (and eventually forecast-

ing) ground EM field due to space weather events. However, our vision of the problem is that each source setting discussed in this study has its own advantages and drawbacks.

The MHD-based approach is the only one out of the considered three, which allows researchers to forecast the space weather impact on ground-based technological systems. This is possible due to the fact that MHD simulations are run on the basis of the satellite solar wind data collected at L1 Lagrange point. The solar wind velocity has typical speed of 300–500 km/s and, thus, the geomagnetic disturbance observed at the Earth's surface is usually lagged compared to L1 point in the range of 30–90 min (Cameron & Jackel, 2019). This time is, obviously, reduced for fast CMEs; the initial speed of one of the fastest recorded CMEs, which occurred on 23 July 2012 (but was not Earth-directed), was estimated as 2500±500 km/s (Baker et al., 2013). Another advantage of the aforementioned method is the ability to compute equivalent current and, subsequently, EM field for any point on the Earth. It is noteworthy that the method is not dependent on ground-based geomagnetic field observations. The drawbacks of the approach is that it is currently the least accurate among the considered modeling techniques. Moreover, significant computational resources (in terms of CPU time and memory) are required to carry out MHD simulations. In spite of the fact that these simulations are still rather far from reproducing actual ground geomagnetic disturbances (as is shown once again in this paper) there are continuing efforts to improve the predictive power of MHD models (e.g., Zhang et al. (2019)).

The SECS-based approach uses ground magnetometers' data and, thus, does not have forecasting capabilities. However, it is the most accurate among all the considered approaches, but in order to properly capture the spatio-temporal evolution of the source it requires a dense grid of continuous geomagnetic field observations in the region of interest.

Plane wave method is most probably an optimal choice for EM modeling (due to space weather events) in low- and mid-latitude regions provided MT impedances are estimated in these regions on as regular and detailed grid as practicable. This, in particular, means that dedicated MT survey in the region of interest is a prerequisite for proper implementation of this method. This approach is the least computationally expensive among the three, as MT impedances can be computed/estimated in advance and then convolved with the magnetic field which, again, requires a network of continuous geomagnetic field observations in the region. However, the violation of the plane wave assumption in the high-latitude leads to less accurate results compared to those obtained with the SECS-based method.

Acknowledgments

This work has been supported by grant 16-17-00121 from the Russian Science Foundation (E.M. and V.P.) and carried out as the state assignment of the Schmidt Institute of Physics of the Earth, Russian Academy of Sciences (E.S.). A.K. has been partially supported by the ESA through the Swarm DISC project. N.K.K's contribution has been partially supported by NOTUR/NORSTOR under project NN9496K. The SWMF model is available from the University of Michigan upon acceptance of license agreement, and SWMF results used here are available at NASA's Community Coordinated Modeling Center (CCMC: `https://ccmc.gsfc.nasa.gov/results/viewrun.php?domain=GM&runnumber=Naomi_Maruyama_011818_1`). OMNI solar wind data were used as an input for this run (`http://omniweb.gsfc.nasa.gov`). We are grateful to Olga Kozyreva and Lisa Rosenqvist for useful discussions over the course of this work. We thank Toivo Korja and Maxim Smirnov for providing the SMAP model. The SMAP model is available via the EPOS portal (`http://mt.bgs.ac.uk/EPOSMT/2019/MOD/EPOSMT2019_3D.mod.json`). We thank the institutes that maintain the IMAGE Magnetometer Array: Tromsø Geophysical Observatory of UiT, the Arctic University of Norway (Norway), Finnish Meteorological Institute (Finland), Institute of Geophysics Polish Academy of Sciences (Poland), GFZ Ger-

man Research Center for Geosciences (Germany), Geological Survey of Sweden (Sweden), Swedish Institute of Space Physics (Sweden), Sodankylä Geophysical Observatory of the University of Oulu (Finland), and Polar Geophysical Institute (Russia). In this paper we also used magnetic field data collected at geomagnetic observatory Saint Petersburg. We thank the Geophysical Center of the Russian Academy of Sciences that supports it and INTERMAGNET (`www.intermagnet.org`) for promoting high standards of magnetic observatory practice.

References

Amm, O. (1997). Ionospheric elementary current systems in spherical coordinates and their application. *J. Geomag. Geoelectr.*, *49*(7), 947–955. doi: 10.5636/jgg.49.947

Bailey, R., Halbedl, T., Schattauer, I., Römer, A., Achleitner, G., Beggan, C. D., ... Leonhardt, R. (2017). Modelling geomagnetically induced currents in mid-latitude Central Europe using a thin-sheet approach. *Ann. Geophys.*, *35*(3), 751–761. doi: 10.5194/angeo-35-751-2017

Bailey, R., Halbedl, T. S., Schattauer, I., Achleitner, G., & Leonhardt, R. (2018). Validating GIC models with measurements in Austria: Evaluation of accuracy and sensitivity to input parameters. *Space Weather*, *16*(7), 887–902. doi: 10.1029/2018SW001842

Baker, D. N., Li, X., Pulkkinen, A., Ngwira, C. M., Mays, M. L., Galvin, A. B., & Simunac, K. D. C. (2013). A major solar eruptive event in July 2012: Defining extreme space weather scenarios. *Space Weather*, *11*(10), 585–591. doi: 10.1002/swe.20097

Beggan, C. D. (2015). Sensitivity of geomagnetically induced currents to varying auroral electrojet and conductivity models. *Earth Planets Space*, *67*(24). doi: 10.1186/s40623-014-0168-9

Beggan, C. D., Beamish, D., Richards, A., Kelly, G. S., & Thomson, A. W. P. (2013). Prediction of extreme geomagnetically induced currents in the UK high-voltage network. *Space Weather*, *11*(7), 407–419. doi: 10.1002/swe.20065

Belakhovsky, V., Pilipenko, V., Engebretson, M., Sakharov, Y., & Selivanov, V. (2019). Impulsive disturbances of the geomagnetic field as a cause of induced currents of electric power lines. *J. Space Weather Space Clim.*, *9*(A18). doi: 10.1051/swsc/2019015

Berdichevsky, M. N., & Dmitriev, V. I. (2008). *Models and methods of magnetotellurics*. Springer, Berlin, Heidelberg. doi: 10.1007/978-3-540-77814-1

Cameron, T. G., & Jackel, B. (2019). Using a numerical MHD model to improve solar wind time shifting. *Space Weather*, *17*(5), 662–671. doi: 10.1029/2019SW002175

Campanya, J., Gallagher, P. T., Blake, S. P., Gibbs, M., Jackson, D., Beggan, C. D., ... Hogg, C. (2019). Modeling geoelectric fields in Ireland and the UK for space weather applications. *Space Weather*, *17*(2), 216–237. doi: 10.1029/2018SW001999

Dimmock, A. P., Rosenqvist, L., Hall, J.-O., Viljanen, A., Yordanova, E., Honkonen, I., ... Sjöberg, E. C. (2019). The GIC and geomagnetic response over Fennoscandia to the 7-8 September 2017 geomagnetic storm. *Space Weather*, *17*(7), 989–1010. doi: 10.1029/2018SW002132

Dimmock, A. P., Rosenqvist, L., Welling, D., Viljanen, A., Honkonen, I., Boynton, R. J., & Yordanova, E. (2020). On the regional variability of dB/dt and its significance to GIC. *Space Weather*, *18*, e2020SW002497. doi: 10.1029/2020SW002497

Divett, T., Ingham, M., Beggan, C. D., Richardson, G. S., Rodger, C. J., Thomson, A. W. P., & Dalzell, M. (2017). Modeling geoelectric fields and geomag-

netically induced currents around New Zealand to explore GIC in the South Island's electrical transmission network. *Space Weather*, *15*(10), 1396–1412. doi: 10.1002/2017SW001697

Divett, T., Mac Manus, D. H., Richardson, G. S., Beggan, C. D., Rodger, C. J., Ingham, M., ... Obana, Y. (2020). Geomagnetically induced current model validation from New Zealand's South Island. *Space Weather*, *18*(8), e2020SW002494. doi: 10.1029/2020SW002494

Grayver, A. V., Munch, F. D., Kuvshinov, A. V., Khan, A., Sabaka, T. J., & Tøffner-Clausen, L. (2017). Joint inversion of satellite-detected tidal and magnetospheric signals constrains electrical conductivity and water content of the upper mantle and transition zone. *Geophys. Res. Lett.*, *44*(12), 6074–6081. doi: 10.1002/2017GL073446

Honkonen, I., Kuvshinov, A., Rastätter, L., & Pulkkinen, A. (2018). Predicting global ground geoelectric field with coupled geospace and three-dimensional geomagnetic induction models. *Space Weather*, *16*(8), 1028–1041. doi: 10.1029/2018SW001859

Ivannikova, E., Kruglyakov, M., Kuvshinov, A., Rastätter, L., & Pulkkinen, A. (2018). Regional 3-D modeling of ground electromagnetic field due to realistic geomagnetic disturbances. *Space Weather*, *16*(5), 476–500. doi: 10.1002/2017SW001793

Juusola, L., Vanhamäki, H., Viljanen, A., & Smirnov, M. (2020). Induced currents due to 3D ground conductivity play a major role in the interpretation of geomagnetic variations. *Ann. Geophys.*, *38*(5), 983–998. doi: 10.5194/angeo-38-983-2020

Kelbert, A. (2020). The role of global/regional Earth conductivity models in natural geomagnetic hazard mitigation. *Surv. Geophys.*, *41*, 115–166. doi: 10.1007/s10712-019-09579-z

Kelbert, A., Balch, C., Pulkkinen, A., Egbert, G., Love, J., Rigler, J., & Fujii, I. (2017). Methodology for time-domain estimation of storm time geoelectric fields using the 3-D magnetotelluric response tensors. *Space Weather*, *15*(7), 874–894. doi: doi:10.1002/2017SW001594

Kelbert, A., & Lucas, G. M. (2020). Modified GIC estimation using 3-D Earth conductivity. *Space Weather*, *18*(8), e2020SW002467. doi: 10.1029/2020SW002467

Kelly, G. S., Viljanen, A., Beggan, C. D., & Thomson, A. W. P. (2017). Understanding GIC in the UK and French high-voltage transmission systems during severe magnetic storms. *Space Weather*, *15*(1), 99–114. doi: 10.1002/2016SW001469

Korja, T., Engels, M., Zhamaletdinov, A. A., Kovtun, A. A., Palshin, N. A., Smirnov, M. Y., ... BEAR Working Group (2002). Crustal conductivity in Fennoscandia – a compilation of a database on crustal conductance in the Fennoscandian Shield. *Earth Planets Space*, *54*, 535–558. doi: 10.1186/BF03353044

Kruglyakov, M., Geraskin, A., & Kuvshinov, A. (2016). Novel accurate and scalable 3-D MT forward solver based on a contracting integral equation method. *Computers and Geosciences*, *96*, 208–217. doi: 10.1016/j.cageo.2016.08.017

Kruglyakov, M., & Kuvshinov, A. (2018). Using high-order polynomial basis in 3-D EM forward modeling based on volume integral equation method. *Geophys. J. Int.*, *213*(2), 1387–1401. doi: 10.1093/gji/ggy059

Kwagala, N. K., Hesse, M., Moretto, T., Tenfjord, P., Norgren, C., Tóth, G., ... Spinnangr, S. F. (2020). Validating the Space Weather Modeling Framework (SWMF) for applications in northern Europe - Ground magnetic perturbation validation. *J. Space Weather Space Clim.*, *10*, 33. doi: 10.1051/swsc/2020034

Linty, N., Minetto, A., Dovis, F., & Spogli, L. (2018). Effects of phase scintillation on the GNSS positioning error during the September 2017 storm at Svalbard.

Space Weather, *16*(9), 1317–1329. doi: 10.1029/2018SW001940

Liu, C., Wang, X., Wang, H., & Zhao, H. (2018). Quantitative influence of coast effect on geomagnetically induced currents in power grids: a case study. *J. Space Weather Space Clim.*, *8*, A60. doi: 10.1051/swsc/2018046

Lucas, G. M., Love, J. J., & Kelbert, A. (2018). Calculation of voltages in electric power transmission lines during historic geomagnetic storms: An investigation using realistic Earth impedances. *Space Weather*, *16*(2), 181–195. doi: 10.1002/2017SW001779

Marshalko, E., Kruglyakov, M., Kuvshinov, A., Murphy, B. S., Rastätter, L., Ngwira, C., & Pulkkinen, A. (2020). Exploring the influence of lateral conductivity contrasts on the storm time behavior of the ground electric field in the eastern United States. *Space Weather*, *18*(2), 159–195. doi: 10.1029/2019SW002216

Marshall, R. A., Wang, L., Paskos, G. A., Olivares-Pulido, G., Van Der Walt, T., Ong, C., ... Yoshikawa, A. (2019). Modeling geomagnetically induced currents in Australian power networks using different conductivity models. *Space Weather*, *17*(5), 727–756. doi: 10.1002/2017SW001793

Myllys, M., Viljanen, A., Rui, O. A., & Ohnstad, T. M. (2014). Geomagnetically induced currents in Norway: the northernmost high-voltage power grid in the world. *J. Space Weather Space Clim.*, *4*, A10. doi: 10.1051/swsc/2014007

Nakamura, S., Ebihara, Y., Fujita, S., Goto, T., Yamada, N., Watari, S., & Omura, Y. (2018). Time domain simulation of geomagnetically induced current (GIC) flowing in 500-kv power grid in Japan including a three-dimensional ground inhomogeneity. *Space Weather*, *16*(12), 1946–1959. doi: 10.1029/2018SW002004

Pankratov, O., & Kuvshinov, A. (2016). Applied mathematics in EM studies with special emphasis on an uncertainty quantification and 3-D integral equation modelling. *Surv. Geophys.*, *37*(1), 109–147. doi: 10.1007/s10712-015-9340-4

Pokhrel, S., Nguyen, B., Rodriguez, M., Bernabeu, E., & Simpson, J. J. (2018). A finite difference time domain investigation of electric field enhancements along ocean-continent boundaries during space weather events. *J. Geophys. Res. Space Phys.*, *123*(6), 5033–5046. doi: 10.1029/2017JA024648

Pulkkinen, A., Lindahl, S., Viljanen, A., & Pirjola, R. (2005). Geomagnetic storm of 29–31 October 2003: Geomagnetically induced currents and their relation to problems in the Swedish high-voltage power transmission system. *Space Weather*, *3*(8), S08C03. doi: 10.1029/2004SW000123

Püthe, C., & Kuvshinov, A. (2013). Towards quantitative assessment of the hazard from space weather. Global 3-D modellings of the electric field induced by a realistic geomagnetic storm. *Earth Planets Space*, *65*, 1017–1025. doi: 10.5047/eps.2013.03.003

Püthe, C., Manoj, C., & Kuvshinov, A. (2014). Reproducing electric field observations during magnetic storms by means of rigorous 3-D modelling and distortion matrix co-estimation. *Earth Planets Space*, *66*, 162-171. doi: 10.1186/s40623-014-0162-2

Rastätter, L., Toth, G., Kuznetsova, M. M., & Pulkkinen, A. (2014). CalcDeltaB: An efficient post processing tool to calculate ground-level magnetic perturbations from global magnetosphere simulations. *Space Weather*, *12*, 553–565. doi: 10.1002/2014SW001083

Rosenqvist, L., & Hall, J. O. (2019). Regional 3-D modeling and verification of geomagnetically induced currents in Sweden. *Space Weather*, *17*(1), 27–36. doi: 10.1029/2018SW002084

Sokolova, E. Y., Kozyreva, O. V., Pilipenko, V. A., Sakharov, Y. A., & Epishkin, D. V. (2019). Space-weather-driven geomagnetic- and telluric-field variability in northwestern Russia in correlation with geoelectrical structure and currents induced in electric-power grids. *Izv. Atmos. Ocean. Phys.*, *55*, 1639–1658. doi:

10.1134/S000143381911015X

Tanskanen, E. I. (2009). A comprehensive high-throughput analysis of substorms observed by IMAGE magnetometer network: Years 1993–2003 examined. *J. Geophys. Res.*, *114*, A05204. doi: 10.1029/2008JA013682

Toffoletto, F., Sazykin, S., Spiro, R., & Wolf, R. (2003). Inner magnetospheric modeling with the Rice Convection Model. In C. A. C.-L. et al. (Ed.), *Advances in space environment research* (pp. 175–196). Springer, Dordrecht. doi: 10.1007/978-94-007-1069-6_19

Toth, G., Sokolov, I., Gombosi, T. I., Chesney, D. R., Clauer, C. R., De Zeeuw, D. L., ... Kota, J. (2005). Space Weather Modeling Framework: A new tool for the space science community. *J. Geophys. Res. Space Phys.*, *110*, A12226. doi: 10.1029/2005JA011126

Toth, G., van der Holst, B., Sokolov, I. V., De Zeeuw, D. L., Gombosi, T. I., Fang, F., ... Opher, M. (2012). Adaptive numerical algorithms in space weather modeling. *J. Comput. Phys.*, *231*(3), 870–903. doi: 10.1016/j.jcp.2011.02.006

van de Kamp, M. (2013). Harmonic quiet-day curves as magnetometer baselines for ionospheric current analyses. *Geosci. Instrum. Method. Data Syst.*, *2*, 289–304. doi: 10.5194/gi-2-289-2013

Vanhamäki, H., & Juusola, L. (2020). Introduction to Spherical Elementary Current Systems. In M. W. Dunlop & H. Lühr (Eds.), *Ionospheric multi-spacecraft analysis tools: Approaches for deriving ionospheric parameters* (pp. 5–33). Cham: Springer International Publishing. doi: 10.1007/978-3-030-26732-2_2

Viljanen, A., & Pirjola, R. (2017). Influence of spatial variations of the geoelectric field on geomagnetically induced currents. *J. Space Weather Space Clim.*, *7*, A22. doi: 10.1051/swsc/2017024

Viljanen, A., Pirjola, R., Prácser, E., Katkalov, J., & Wik, M. (2014). Geomagnetically induced currents in Europe – Modelled occurrence in a continent-wide power grid. *J. Space Weather Space Clim.*, *4*, A09. doi: 10.1051/swsc/2014006

Viljanen, A., Pirjola, R., Prácser, E., Ahmadzai, S., & Singh, V. (2013). Geomagnetically induced currents in europe: Characteristics based on a local power grid model. *Space Weather*, *11*(10), 575–584. doi: 10.1002/swe.20098

Viljanen, A., Pirjola, R., Wik, M., Ádám, A., Prácser, E., Sakharov, Y., & Katkalov, J. (2012). Continental scale modelling of geomagnetically induced currents. *J. Space Weather Space Clim.*, *2*, A17. doi: 10.1051/swsc/2012017

Wang, L., Duan, J., Hitchman, A. P., Lewis, A. M., & Jones, W. V. (2020). Modeling geoelectric fields induced by geomagnetic disturbances in 3D subsurface geology, an example from southeastern Australia. *J. Geophys. Res. Solid Earth*, *125*(9), e2020JB019843. doi: 10.1029/2020JB019843

Wang, L., Lewis, A. M., Ogawa, Y., Jones, W. V., & Costelloe, M. T. (2016). Modeling geomagnetic induction hazards using a 3-D electrical conductivity model of Australia. *Space Weather*, *14*, 1125–1135. doi: 10.1002/2016SW001436

Zhang, B., Sorathia, K. A., Lyon, J. G., Merkin, V. G., Garretson, J. S., & Wiltberger, M. (2019). GAMERA: A three-dimensional finite-volume MHD solver for non-orthogonal curvilinear geometries. *The Astrophysical Journal Supplement Series*, *244*(1), 20. doi: 10.3847/1538-4365/ab3a4c

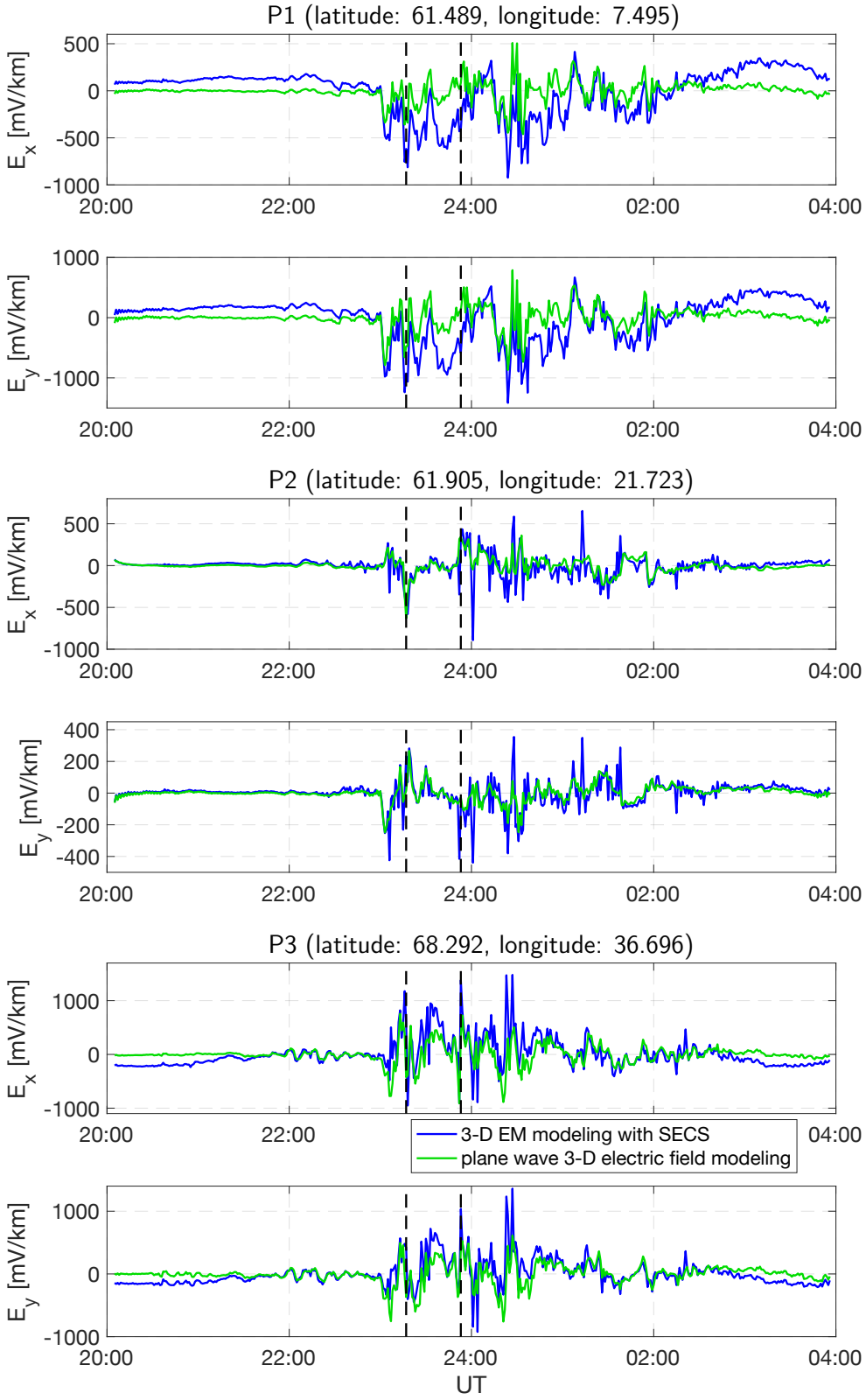

Figure 7. SECS- and plane-wave-based GEF modeling results at three "sites" located in the regions with high lateral conductivity contrasts; locations of these sites are shown in Figure 1.

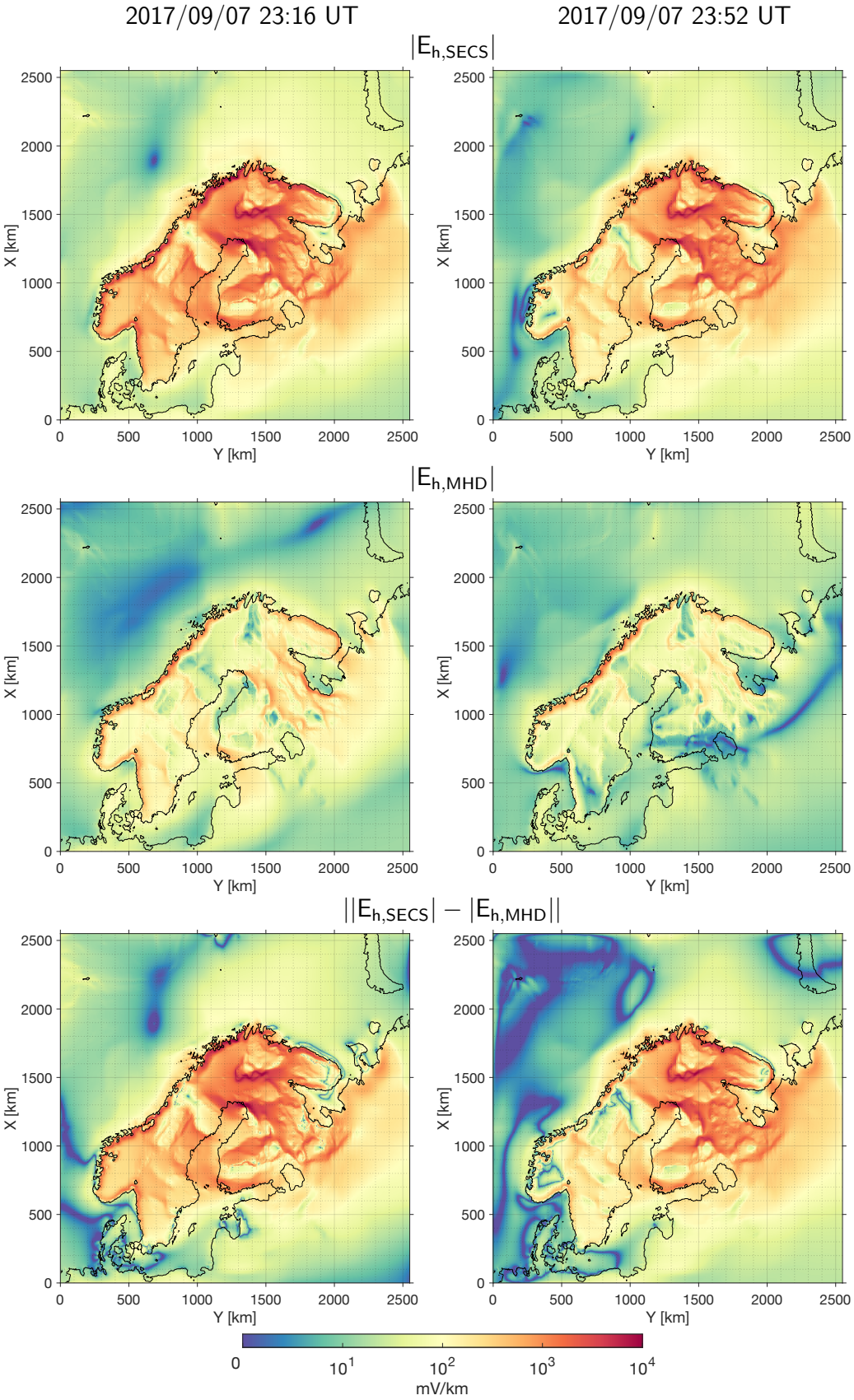

Figure 8. Top and middle: magnitudes of respective SECS- and MHD-based GEF. Bottom: absolute differences between corresponding GEF magnitudes.

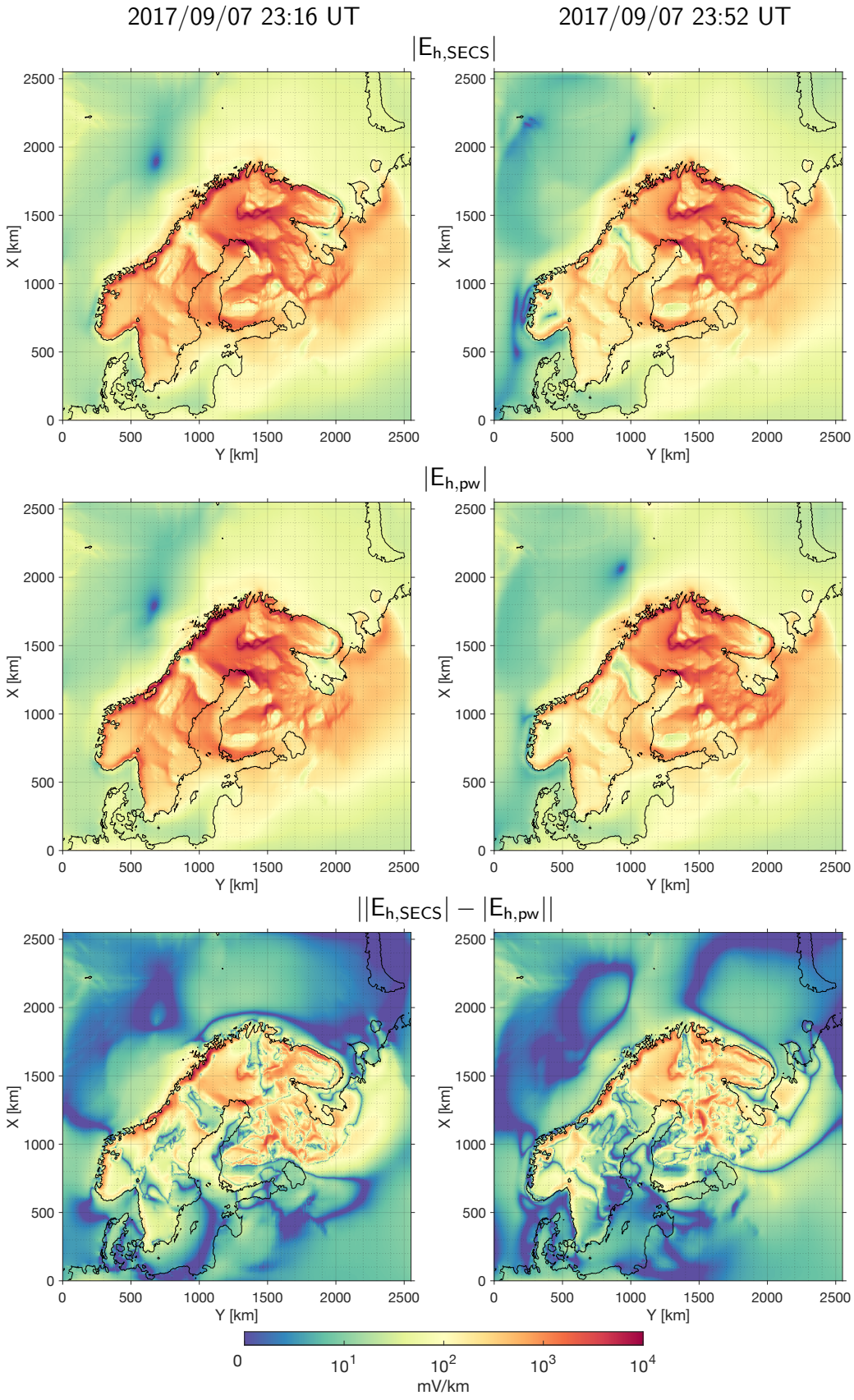

Figure 9. The same legend as in Figure 8 but for SECS- and plane-wave-based GEF.